

## CFD simulation of vortex-induced vibration of free-standing hybrid riser

Yi Cao<sup>\*1</sup> and Hamn-Ching Chen<sup>2a</sup>

<sup>1</sup>Department of Ocean Engineering, Texas A&M University, USA

<sup>2</sup>Zachry Department of Civil Engineering, Texas A&M University, USA

(Received June 29, 2017, Revised August 22, 2017, Accepted August 27, 2017)

**Abstract.** This paper presents 3D numerical simulations of a Free Standing Hybrid Riser under Vortex Induced Vibration, with prescribed motion on the top to replace the motion of the buoyancy can. The model is calculated using a fully implicit discretization scheme. The flow field around the riser is computed by solving the Navier-Stokes equations numerically. The fluid domain is discretized using the overset grid approach. Grid points in near-wall regions of riser are of high resolution, while far field flow is in relatively coarse grid. Fluid-structure interaction is accomplished by communication between fluid solver and riser motion solver. Simulation is based on previous experimental data. Two cases are studied with different current speeds, where the motion of the buoyancy can is approximated to a 'banana' shape. A fully three-dimensional CFD approach for VIV simulation for a top side moving Riser has been presented. This paper also presents a simulation of a riser connected to a platform under harmonic regular waves.

**Keywords:** 3D simulation; free standing hybrid riser; deep water; CFD simulation; vortex-induced vibration; uverset grid

### 1. Introduction

As oil and gas exploration and production activities are focusing more on deep waters, free standing and hybrid risers are finding its applications in these fields all over the world increasingly. The first FSHR was developed and deployed in the Campos Basin in Brazil in Oct. 2007. In Dec. 2009 and early 2010, the first five disconnectable FSHRs were successfully deployed for the Cascade and Chinook field development in the Gulf of Mexico. Since then, the FSHR concept has been widely recognized within the deep-water offshore industry.

Free Standing Hybrid Riser (FSHR) is capable of transferring fluids from seabed to a floating vessel and vice versa, with little influences of environmental loads and vessel motions (Pereira *et al.* 2005, Song *et al.* 2010). A typical system of FSHR is shown in Fig. 1. FSHR consists of a vertical steel pipe tensioned by a submerged buoyancy can. The top of the riser is connected to a buoyancy can which links the production platform using a flexible jumper. The bottom of the riser is attached to a seabed foundation and a rigid jumper connects the FSHR to the pipeline end termination.

---

\*Corresponding author, M.S., E-mail: cyneo41@gmail.com

<sup>a</sup> Professor

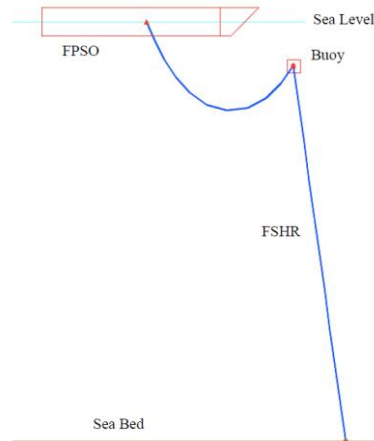


Fig. 1 Free Standing Hybrid Riser System

There are many benefits of FSHR in deep water. First of all, FSHR can be installed before or after the floating production unit is anchored on site. This offers a greater flexibility with respect to time during installation. Secondly, because the riser is tensioned by the air can, it can support its own weight. Therefore, the production platform doesn't need to carry the heavy payloads, in deep water situations. Although there are various versions of the FSHR and the configuration has been modified many times, the key technical benefit of this concept remains that the rigid vertical riser is decoupled from the floating production unit (FPU). The connection is achieved through a flexible jumper. Hence the riser is insensitive to the fatigue caused by the motion of the FPU. Since the fatigue design of the deep-water risers has always been a big challenge, the decoupling effect improves FSHR performance significantly. Numerous FSHR systems have been installed in West coast of Africa in the past few years.

The research of the vortex induced motion of FSHR has been conducted through experiments. Tow tank experiments have been conducted by Wilde (2007) to study the VIV response of a FSHR. The experiments were performed in MARIN's Depressurized Towing Tank facility, which has dimension of 240 m in length, 18 m in width and 8 m in depth. The overhead carriage can maintain an accurate speed between 0 and 8 m/s. The free standing riser model was towed by the carriage using a 200 kg clump weight, hanging from the carriage on 4 steel wires at approximately 7 m water depth. The riser model was mounted at its bottom with a uni-joint on the clump weight. The FSHR model was tested in uniform current conditions with virtually no background turbulence. VIV responses of the riser and buoyancy at different uniform current conditions are observed.

Due to the development of computational techniques, numerical simulation has played an increasingly significant role in offshore VIV problems recently, which is also considered as a valuable alternative to experiments. Rakshit *et al.* (2008), using CFD, simulated a long slender riser, made of composite materials and subject to an ocean current. They studied the influence of the number of modes as well as the influence of mass ratios and the value of the damping coefficient. They found that the vibration amplitude increases with the number of modes. A 3D riser VIV analysis methodology has been developed by Pontaza *et al.* (2005, 2006). A Finite-Analytic Navier Stokes (FANS) algorithm is used to simulate the flow field near the riser. The method uses overset

grid to discretize the flow field and the riser. The results match with the experiments data. A vertical riser VIV simulation in uniform current was conducted by Huang *et al.* (2007). Their simulation results were compared with the experimental data. It is concluded that the present CFD method is capable of providing reasonable results and is suitable for 3D riser VIV analysis in deep water and complex current conditions.

In recent years, numerical methods took part in the analysis of FSHR. Cheng *et al.* (2006, 2007) presented time domain riser VIV research using ABAVIV code. Based on these studies, Liu *et al.* (2009) presented a research of time domain VIV analysis of a FSHR. The analysis was performed using a time domain VIV code ABAVIV, which uses ABAQUS to calculate the response from the VIV forcing. This is the first application of this method to a FSHR.

Although riser VIV CFD simulation is quite popular these days, researches about FSHR VIV have not been fully studied. A 3D numerical simulation for a free standing hybrid riser under interactions is presented in this paper. We use a prescribed motion on the top of the riser to replace the oscillation of the buoyancy can. Finite element method was applied to the model using a fully implicit discretization scheme (Huang *et al.* 2011). The flow field around riser is computed by solving the incompressible Navier-Stokes equations numerically. Overset grid approach is adopted to generate the numerical grids. Fluid-structure interaction is accomplished by communication between fluid solver and riser motion solver. The motion solver inputs drag and lift forces calculated by fluid solver and calculate the displacements in in-line and cross-flow directions. Then motion solver outputs new positions of the riser back to fluid solver.

Simulation is based on the experimental data from the model test of Wilde (2007). Riser particulars used in the simulation are the same as the parameters provided by the experiment. Two cases with different current speeds were simulated and analyzed.

## 2. Numerical approach for riser VIV simulation

This section demonstrates the numerical approach for the riser VIV simulations, including computational fluid dynamics method, motion solver development and fluid-structure interactions.

The numerical approach we adopted is a Finite-Analytic Navier-Stokes (FANS) code. This time domain simulation code can calculate the flow field around the riser by solving the unsteady, incompressible Navier-Stokes equations numerically. The turbulent flow was solved using Large Eddy Simulation (LES) model. The code has been previously validated through multiple applications (Chen *et al.* 1988, 1989, 1990, 2013, Pontaza *et al.* 2005, 2006, Huang *et al.* 2007, 2008, 2011, 2012).

### 2.1 Flow field solver

Finite-Analytic Navier-Stokes (FANS) approach of Chen *et al.* (1990) and Pontaza *et al.* (2005) is employed to solve the unsteady incompressible Navier-Stokes equation. The computational domain is discretized into small numerical elements. FANS method solves a local-analytic solution of governing equation and applies it to each numerical element locally. Large Eddy Simulation (LES) method is used to model the turbulence in the flow field where high frequency fluctuations were filtered out using volume averaging.

Large Eddy Simulation (LES):

$$\frac{\partial \bar{u}_i}{\partial t} + \frac{\partial}{\partial x_j} (\bar{u}_i \bar{u}_j) = -\frac{1}{\rho} \frac{\partial \bar{p}}{\partial x_i} + \nu \frac{\partial^2 \bar{u}_i}{\partial x_i \partial x_j} - \frac{\partial \tau_{ij}}{\partial x_i} \quad (1)$$

Where the subgrid-scale stresses  $\tau_{ij}$  are given by the Smagorinsky subgrid-scale turbulence model

$$\tau_{ij} = \overline{u_i u_j} - \bar{u}_i \bar{u}_j; \quad \tau_{ij} = -2\nu_T \bar{S}_{ij}; \quad \nu_T = (C_S \Delta)^2 \sqrt{2\bar{S}_{ij} \bar{S}_{ij}} \quad (2)$$

## 2.2 Overset grid

In this research, we use two computational blocks to simulate the whole fluid domain: near body grid and wake grid. A typical cross section of this approach is shown in Fig. 2. The near body grid (red) is generated in polar coordinate. Wall boundary condition is applied surround the surface of the riser. Wake grid (green) is generated in Cartesian coordinate right surrounding the near body grid.

The grid has very good concentration around the near body grid. While at far field area, the grid is relatively coarse. This grid distribution provide adequate resolution in the computational domain for vortex shedding and can save more computation effort than the uniform grid. At the interface between near grid and wake grid, we make the sizes of the grid from each block of the same magnitude in order to guarantee the accuracy of the communication of the flow field information.

A dynamic grid scheme (a moving grid) is also employed in this approach. As the riser moves, the near body grid and wake grid will move with the riser at the same velocity. This synchronous movement guarantees that there is no gap between the riser boundary and fluid boundary. Through moving grid, we eliminate the need to generate a grid at each time step, which is a time consuming process of CFD calculation. We only need to move the existing blocks and determine the new interaction between two blocks.

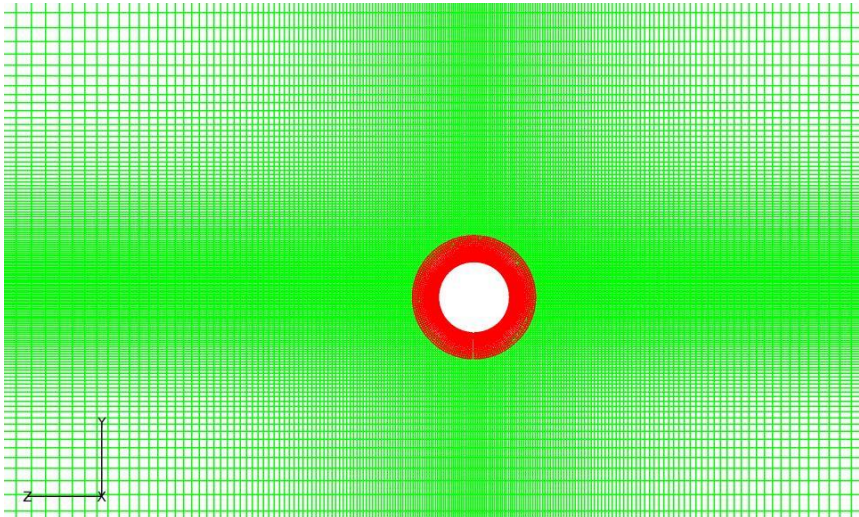


Fig. 2 2D Cross Section Grid for VIV Simulation

### 2.3 Motion solver

A riser can be modeled as a tensioned beam in the in-line and cross-flow directions separately. The tension distribution varies linearly in the axial direction. In reality, the top tensioned risers have the highest tension at the top, and lowest tension at the bottom due to its own submerged weight. The governing equations of a tensioned beam are described as

$$T \frac{d^2 y}{dx^2} + \frac{dy}{dx} \frac{dT}{dx} - \frac{d^2}{dx^2} \left( EI \frac{d^2 y}{dx^2} \right) + F_y = M \ddot{y} + D_s \dot{y} \quad (3)$$

$$T \frac{d^2 z}{dx^2} + \frac{dz}{dx} \frac{dT}{dx} - \frac{d^2}{dx^2} \left( EI \frac{d^2 z}{dx^2} \right) + F_z = M \ddot{z} + D_s \dot{z} \quad (4)$$

Where  $T$  is the axial tension,  $F_y$  and  $F_z$  are the external forces in  $y$  and  $z$  directions,  $x$  is the axial direction,  $y$  is the in-line direction,  $z$  is the cross-flow direction,  $E$  is Young's modulus,  $I$  is the area moment of inertia,  $D_s$  is the damping ratio and  $M$  is the mass of riser in unit length. A finite difference scheme (Huang *et al.* 2011, Xiao 2015) was adopted to discretize the governing equation. The discretization results are presented as

$$\begin{aligned} & \frac{EI}{\Delta x^4} y_{j-2}^n - \left( \frac{T_j}{\Delta x^2} - \frac{1}{2\Delta x} \frac{dT_j}{dx} + \frac{4EI}{\Delta x^4} \right) y_{j-1}^n + \left( \frac{2T_j}{\Delta x^2} + \frac{6EI}{\Delta x^4} + \frac{M}{\Delta t^2} + \frac{D_s}{\Delta t} \right) y_j^n \\ & - \left( \frac{T_j}{\Delta x^2} - \frac{1}{2\Delta x} \frac{dT_j}{dx} + \frac{4EI}{\Delta x^4} \right) y_{j+1}^n + \frac{EI}{\Delta x^4} y_{j+2}^n \\ & = F_{y_j}^n + \left( \frac{2M}{\Delta t^2} + \frac{D_s}{\Delta t} \right) y_j^{n-1} - \frac{M}{\Delta t^2} y_j^{n-2} \end{aligned} \quad (5)$$

$$\begin{aligned} & \frac{EI}{\Delta x^4} z_{j-2}^n - \left( \frac{T_j}{\Delta x^2} - \frac{1}{2\Delta x} \frac{dT_j}{dx} + \frac{4EI}{\Delta x^4} \right) z_{j-1}^n + \left( \frac{2T_j}{\Delta x^2} + \frac{6EI}{\Delta x^4} + \frac{M}{\Delta t^2} + \frac{D_s}{\Delta t} \right) z_j^n \\ & - \left( \frac{T_j}{\Delta x^2} - \frac{1}{2\Delta x} \frac{dT_j}{dx} + \frac{4EI}{\Delta x^4} \right) z_{j+1}^n + \frac{EI}{\Delta x^4} z_{j+2}^n \\ & = F_{z_j}^n + \left( \frac{2M}{\Delta t^2} + \frac{D_s}{\Delta t} \right) z_j^{n-1} - \frac{M}{\Delta t^2} z_j^{n-2} \end{aligned} \quad (6)$$

$\Delta t$  is the time step, and  $n$  denotes the time step.  $\Delta x$  is the length of a riser's segment. In this research, we discretize the riser into 250 segments. The discretization is applied for both in-line and cross-flow direction. Parameters  $T$ ,  $EI$ ,  $M$ ,  $D_s$  are declared through the riser input file. External forces  $F_y$  and  $F_z$  are obtained from the fluid solver. And the riser displacements at each node are computed by the motion solver.

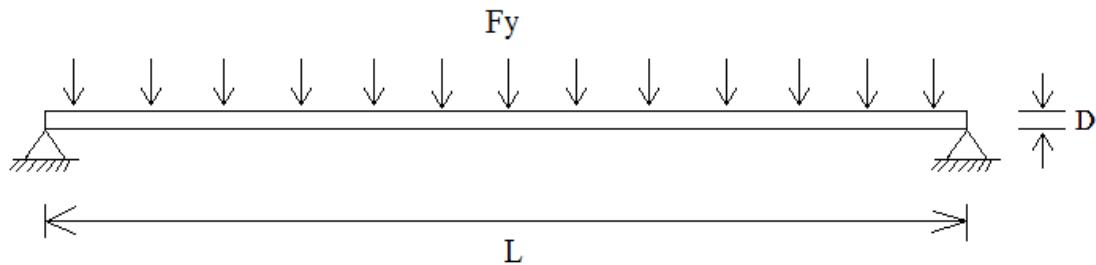


Fig. 3 Static Validation Case for Pipeline Motion Solver

In order to verify the accuracy of this riser motion solver, we check two cases against the theoretical solution: (1) a riser with constant tension, (2) a riser with linearly distributed tension. In reality, the riser is standing vertically, with the tension on the top provided by the buoyancy can and the tension at the bottom provided by the base structure. Due to its own submerged weight, the tension is highest on the top and lowest at the bottom. The results are shown in the Figs. 4 and 5.

For constant tension case, the riser displacement is symmetric and the maximum deflection occurs in the middle of the riser. As for the varying tension case, the displacement is not symmetric and the maximum riser deflection occurs somewhere in the lower portion of the riser. For both cases, our motion solver's solution exactly follows the theoretical solution.

Another case to verify the motion solver is set in dynamical conditions. Fig. 6 demonstrates the case. A riser with constant tension has one end pinged to the wall and the other end moving in a prescribed motion.

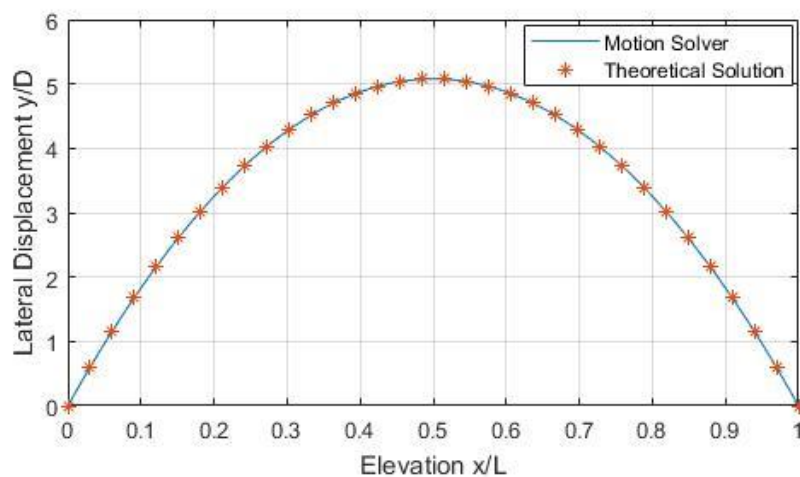


Fig. 4 Riser Static Displacement Comparison (Constant Tension)

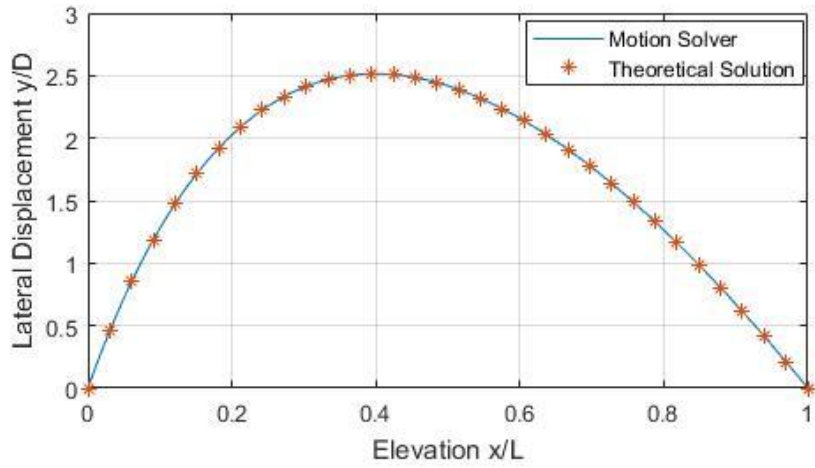


Fig. 5 Riser Static Displacement Comparison (Varying Tension)

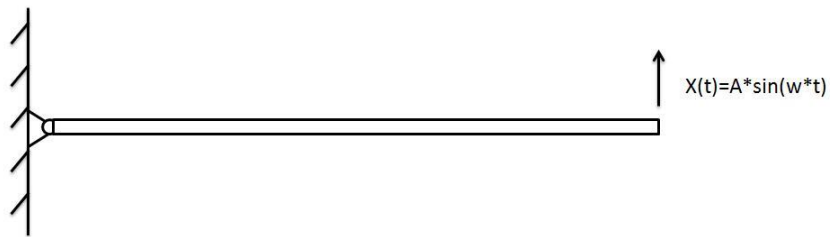


Fig. 6 Dynamic Validation Case for Riser Motion Solver

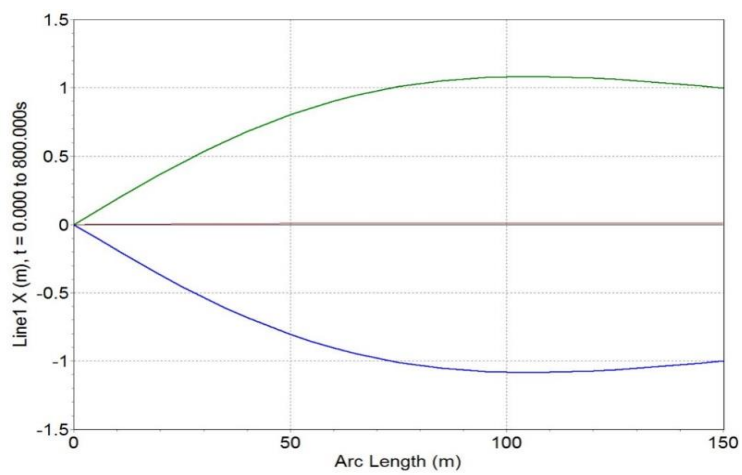


Fig. 7 Riser Envelope by OrcaFlex

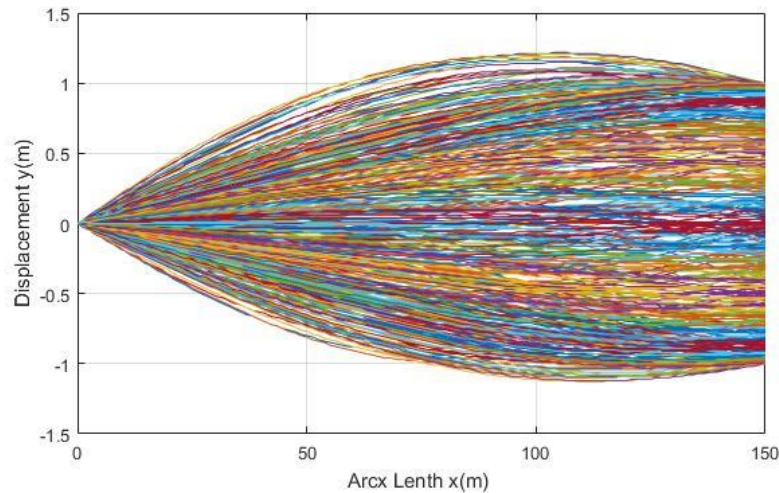


Fig. 8 Riser Envelope by Motion Solver

The prescribed motion we impose at the free end of the riser is following  $X(t)=A*\sin(\omega t)$ .  $A$  is the amplitude of the motion, and  $\omega$  implies the frequency of the movement. We use commercial software OrcaFlex, a package for dynamic analysis of offshore marine systems, to do the comparison.

At a specific tension, length, Young's modulus and movement frequency, the vibration envelope has the shape shown in Fig. 7, which is generated by OrcaFlex. The result computed by our motion solver is shown in Fig. 8. The two comparisons agree with each other.

#### 2.4 CFD simulation procedures

Fluid-structure interaction problems and multi-physics problems are usually too complex to solve analytically. These problems are dealt with using experiments or numerical simulation. The maturity of computational fluid dynamics has enabled numerical simulation of fluid-structure interaction. There are two main approaches that exist for the FSI problems: Monolithic approach and Partitioned approach.

The method we adopted in this research is partitioned approach: the equation governing the flow and the displacement of the riser are solved separately in two distinct solvers. At each time step, the fluid solver, based on the displacement information of the riser, solves the Navier-Stokes equation numerically and obtain the pressure and force of the whole flow field. Drag and lift forces are then read by riser motion solver as input to calculate the new position for next step computation. In this way, the FSI problem is solved in a partitioned approach.

### 3. VIV simulation of a FSHR

During the last decades, many VIV experiments have being performed and published on deep water slender bodies. However, the research especially focused on the Free Standing Hybrid Riser

is relatively rare. Wilde (2007) did model tests on the VIV of the air can of a Free Standing Riser System in current. The experiment was carried out at MARIN (Maritime Research Institute Netherlands), in the depressurized towing tank. In our research, we use Wilde's experimental results to benchmark our computer codes.

### 3.1 Experiment background

The experiments were carried out in a towing tank, being 240 m long, 18 m wide and 8 m deep. As shown in Fig. 9, the tank has an overhead carriage which can control accurate speed between 0 and 8 m/s. the riser model was mounted at its bottom connected to the clump through the uni-joint. The riser was also tensioned by the air can at the top. As the carriage moves at certain speed, the whole system moves together, including the riser. This simulate the situation that riser is under uniform current.

The riser model diameter is 0.008 m and the length over diameter is  $L/D = 625$ , which indicates a very long riser. The other parameters are provided in the following Tables. Table 1 provides information for the buoyancy can and Table 2 provides particulars for the vertical riser. A geometrical model scale of 1:68.75 was assumed. Froude scaling was used for the velocities, accelerations and loads.

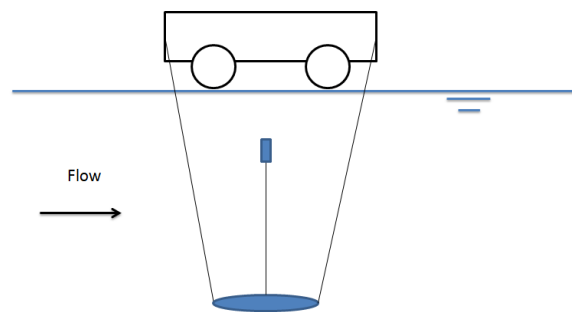


Fig. 9 Test Setup

Table 1 Parameters of air can

Parameter	Symbol	Model Scale	Full Scale
Diameter	OD	80 mm	5.5 m
Length	L	495 mm	34.0 m
Weight in air	m	867 gr	2,833 KN
Mass ratio	m+	0.35	0.35
Upward thrust	T	1,621 gr	5,167 KN

Table 2 Parameters of vertical riser

Parameter	Symbol	Model Scale	Full Scale
Diameter	OD	8 mm	550 mm
Wall thickness	T	1 mm	69 mm
Length	L	5 m	344 m
Young's modulus	E	3,000 N/mm <sup>2</sup>	2.1E11 N/m <sup>2</sup>
Bending stiffness	EI	0.412 Nm <sup>2</sup>	3.25E8 Nm <sup>2</sup>
Weight in air	m	64 gr/m	439 kg/m
Underwater weight	W	0.41 N/m	1,922 N/m
Tension on the top	$T_{up}$	5,167 KN	4505.832 KN

In this paper, the buoyancy can movement was replaced by the prescribed motion on the top of the riser. The trajectory of the air can is shown in Fig. 10. As we can see, the motions of the air can at current speed 0.5 m/s and 0.83 m/s (full scale) are in 'banana' shape. At current speed 0.5 m/s, the cross-flow VIV response of the buoyancy can is slightly less than the diameter of the air can ( $A/D \sim 0.9$ ). The in-line VIV response is about 0.15 riser diameters.

In our computational grid,  $y$  is the in-line direction,  $z$  is the cross-flow direction. So we fit the displacement pattern as follows

$$z(t) = A_z \sin(\omega t) \quad (7)$$

$$y(t) = A_y \sin(2\omega t + \theta) \quad (8)$$

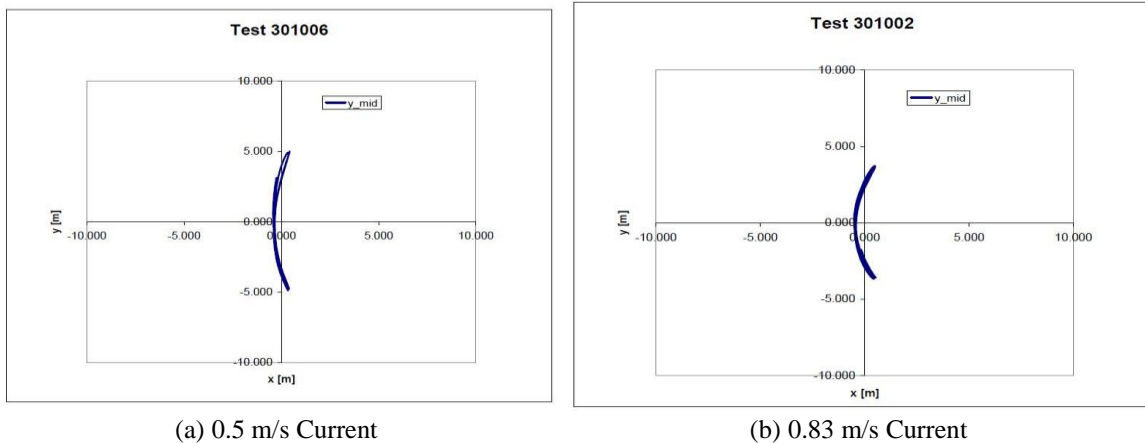


Fig. 10 Buoyancy Can Trajectory, Wilde (2007)

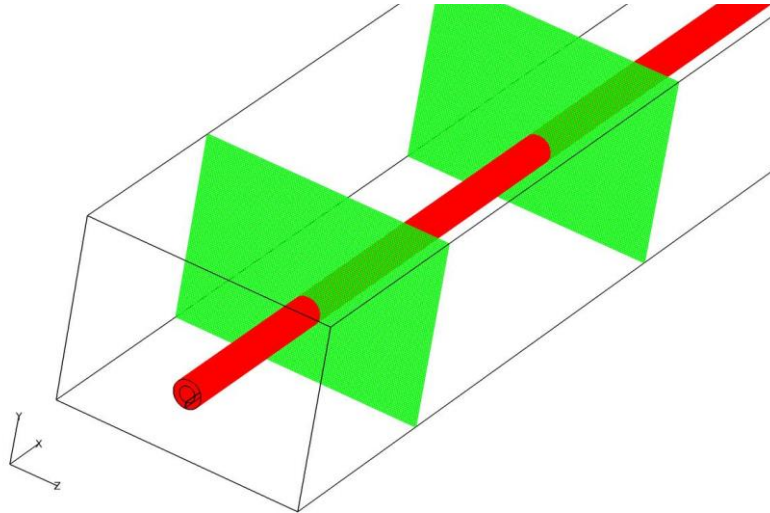


Fig. 11 Overview of Fluid Domain for an Isolated Riser

$A_z$  is the average cross-stream amplitude of vibration.  $A_x$  is the average in-line amplitude of vibration.  $\omega = 2\pi f_y$ , with  $f_y/f_z = 2$ ,  $\theta$  is the phase angle. For different phase angles the trajectory will present different “figure of eight” shapes.

The frequencies obtained from the experiment are 0.0132 Hz for current speed 0.5 m/s and 0.0191 Hz for current speed 0.83 m/s. Phase angle  $\theta = \pi/2$  for the final fit we adopted.

### 3.2 Grid generation

As discussed before, an overset grid scheme is adopted in our research. For an isolated riser in infinite fluid domain, we use two blocks of grid: near body grid and wake grid. Fig. 11 shows the wake grid with the near body grid implanted inside. Red block consists of 373100 ( $50 \times 182 \times 41$ ) grid points and green block consists of 1593050 ( $50 \times 151 \times 211$ ) grid points. There are about 2 million computational nodes in this simulation. The axial direction is divided into 50 layers and the length over diameter is 625.

The two-dimensional view of the cross section is presented in Fig. 12. The riser is placed in the middle of the fluid domain. The riser center was set at the origin point  $(y, z) = (0, 0)$ . The flow inlet (bottom side) is 8 D in front of the riser, while the flow outlet is 16 D behind the riser. Since we have prescribed “banana shape” motion, we make the lateral sides 16 D apart from the riser. The uniform current propagates in the positive  $y$  direction (in-line direction).

The red area is the near body grid, rather than the riser cross section. Fig. 13 provides a close up view of the red grid. The inner boundary of the red grid is the riser outer boundary. And the red loop grid represents flow field around the riser. The near body grid consists of  $50 \times 182 \times 41$  grid points, with 49 elements in axial direction, 180 elements in circumferential direction and 40 elements in radial direction. In circumferential direction, 182 grid points create only 180 elements because node #182 overlap with node #2, while node #181 overlap with node #1. This overlapping allows flow information communication between these grid nodes.

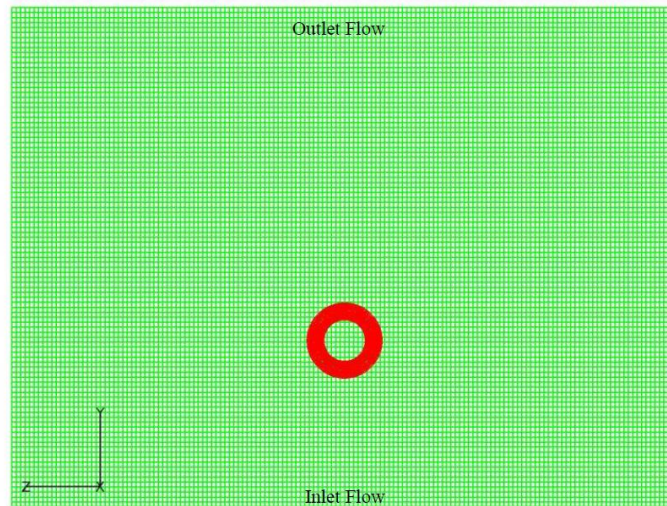


Fig. 12 Cross Section of Fluid Domain

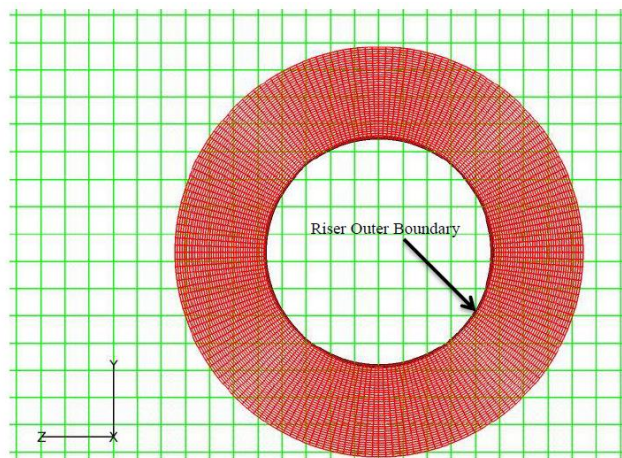


Fig. 13 Near Body Grid

The grid generated above is uniformly distributed. It works well when the simulation domain is small. However, when you are specifying a large domain, there will be too many grid points inside the domain, which will cost tremendous calculation time. To solve this problem, we need to re-spline the grid. As we can imagine, the area surrounding the riser will have flow changing dramatically. For this area, a finer grid is needed. As for the far way field, the grid can be relatively coarse. The re-splined grid is presented in Figs. 14 and 15. In near wall block, the size of the innermost element is  $0.001 D$ , while the outmost one is of  $0.035 D$ . In the wake block, the finer grid is situated at the riser center and vice versa. The size of wake grid elements ranges from  $0.025 D$  to  $0.8 D$  in  $y$  direction and  $0.025$  to  $0.3 D$  in  $z$  direction.

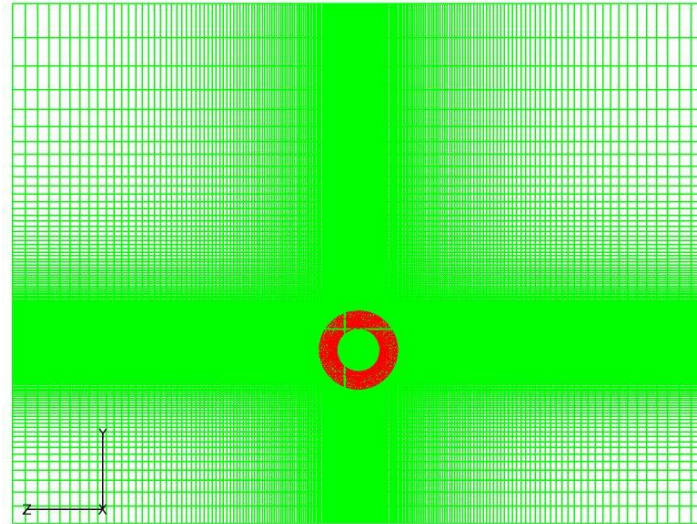


Fig. 14 Overview of the Re-splined Grid

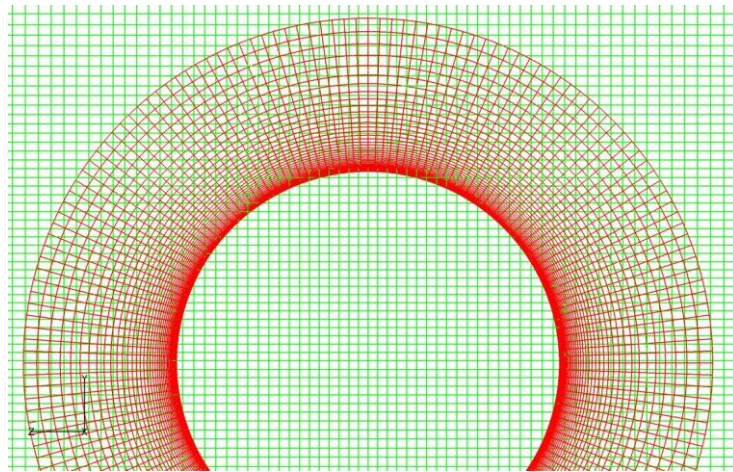


Fig. 15 Near View of The Re-splined Grid

Whether the near body grid size at the outer boundary and the nearby wake grid size are close to each other, is essential to the interpolation between two grid sets. In Fig. 16, red and green elements are about the same size. Red node 1 inside the green element ABCD, can receive flow information by interpolating the value of node A, B, C and D. Similarly, green node B can receive information from red nodes 1, 2, 3 and 4. This is how two blocks communicate with each other. A bad interpolation is shown in Fig. 17. The size of the outer boundary of the red grid is too small and the nearby wake grid is too big. There will be many red points inside one green element and linear interpolation can't guarantee each point receive true value of flow field information, especially when the flow changes dramatically in this element.

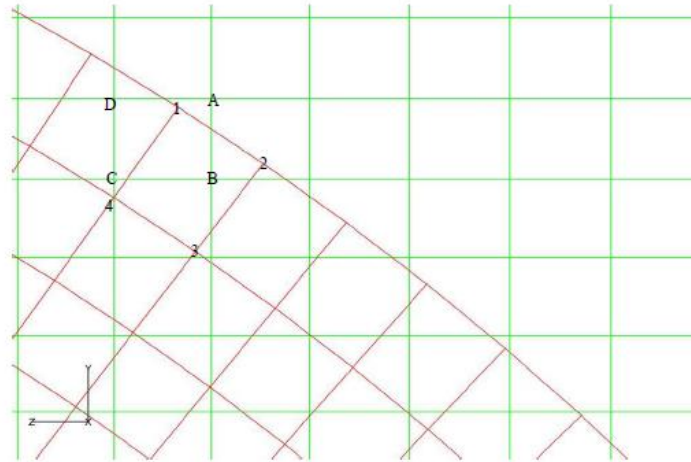


Fig. 16 Interpolation Between Two Blocks

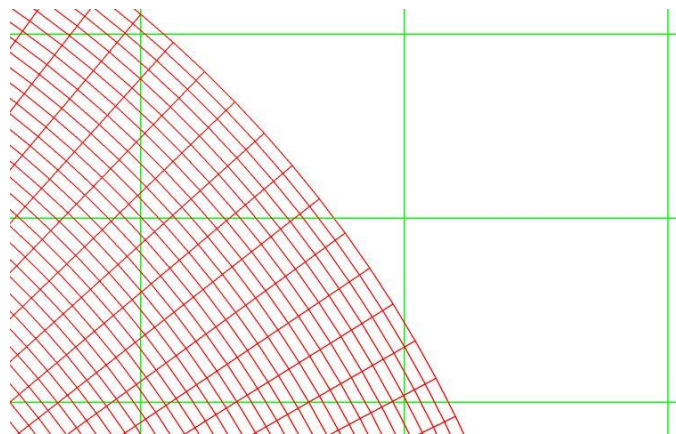


Fig. 17 Bad Interpolation Between Two Blocks

Although there are only 50 elements for the flow solver, the riser is divided into 250 segments in the motion solver. The drag and lift forces are linearly interpolated for the calculation of riser in-line and cross-flow displacement.

### 3.3 Simulation results

The simulations were performed under current speeds of 0.5 m/s and 0.83 m/s in the full-scale settings. The Reynold number range is between  $2.3 \times 10^5$  and  $4.0 \times 10^5$ . At the beginning, the riser was set straight, vertically standing in the still water. When the simulation starts, vortex starts to generate around the riser due to the current. Meanwhile, the top of the riser start to oscillate according to the prescribed motion. At the same time, the riser begins deflection in in-line direction.

A close look at the fixed end of the riser, shows the evolution of the vortex in the uniform current, as was shown in Fig. 18.

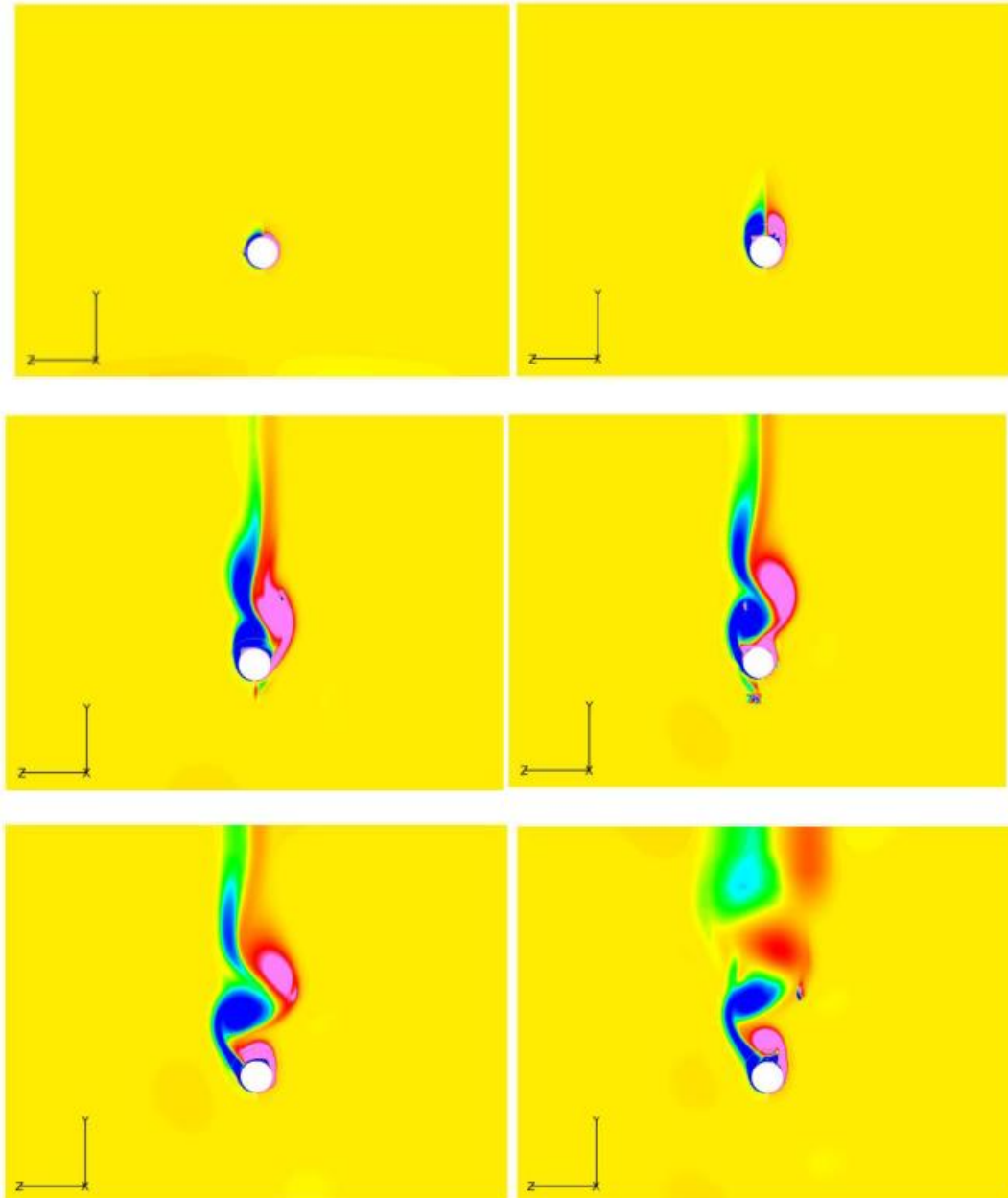


Fig. 18 Vortex Evolution at Riser Bottom ( $U = 0.50$  m/s)

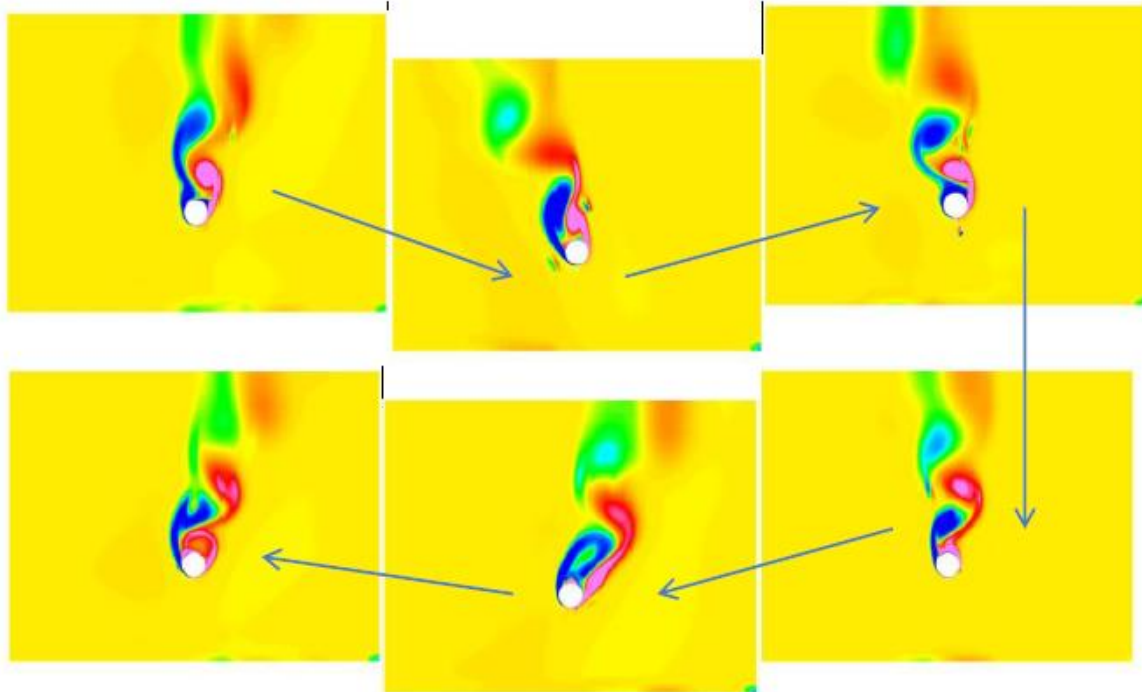


Fig. 19 Motion at Riser Top ( $U = 0.50$  m/s)

Fig. 19 shows the motion at the top of the riser and the vortex generated. At both sides of the “banana shape”, the riser velocity is zero and only uniform current coming in positive  $y$  direction. The vortex generated at these two ends sheds in  $y$  direction. The velocity reaches maximum at the middle of the “banana” shape. The vortex sheds in the direction of the relative velocity.

The deflection of the riser is presented in Fig. 20. Under the current speed 0.5 m/s and 0.83 m/s, for both in-line and cross-flow, the deflection is small. The largest displacement occurs at the top of the riser. We can clearly observe the “banana shape” motion in  $y$ - $z$  plane at the top of the riser. The envelope of the displacement is shown in Fig. 21. The results agree with the experimental data concluding that, at low current speed (0.5 m/s & 0.83 m/s), regular mode 1 is the dominant response.

The riser displacement history in the in-line and cross-flow directions at current speed 0.83 m/s is shown in Figs. 22 and 23 separately. The top sections are mostly subject to the prescribed motion. Thus, we choose the near bottom displacement as a representative. It should be noted that the prescribed motion is simulated in an equivalent stable status, which means the riser will oscillate near origin point ( $y = 0, z = 0$ ) in both in-line and cross-flow direction. The time increment for each simulation step is 0.1 s.

Fast Fourier Transform was applied to study the frequency of the vibration in cross-flow direction. To avoid the influence of the initiation, we use the data from time=500s to time=2000s. The result is presented in Fig. 24. As we can observe, the first peaks for two current speeds occur near 0.02 Hz.

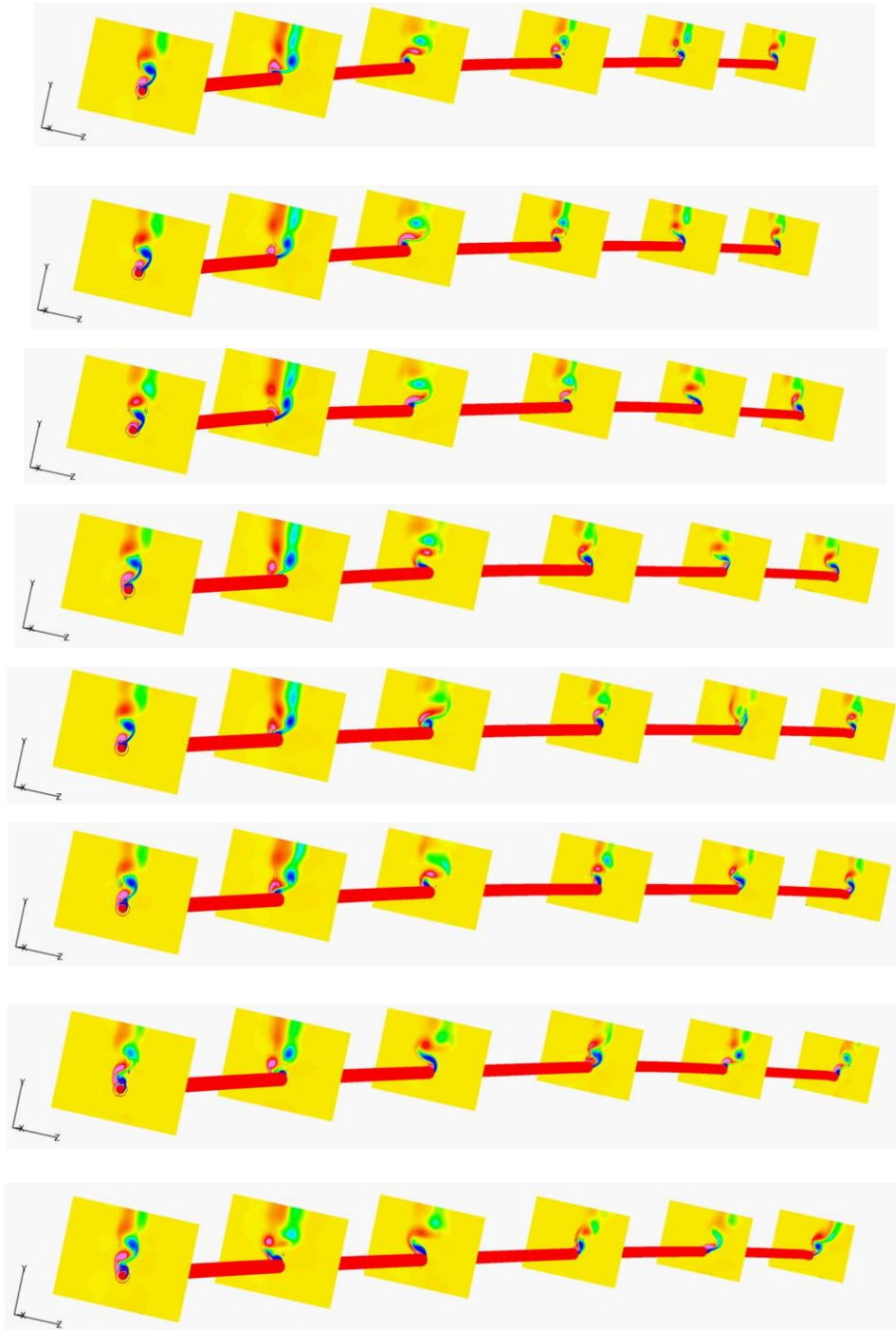


Fig. 20 Riser Deflection ( $U = 0.50$  m/s)

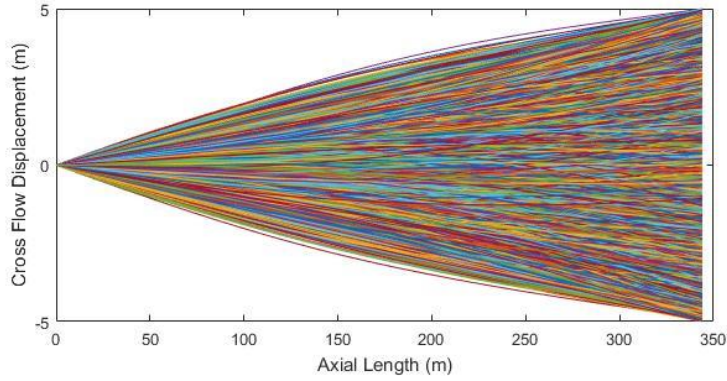


Fig. 21 Displacement Envelope

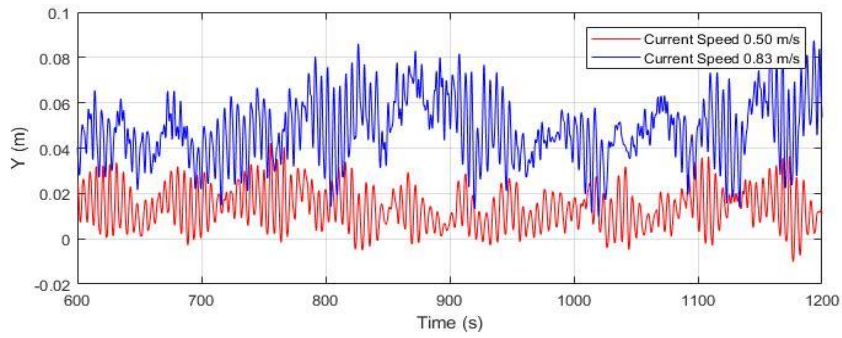


Fig. 22 In-line Motion History

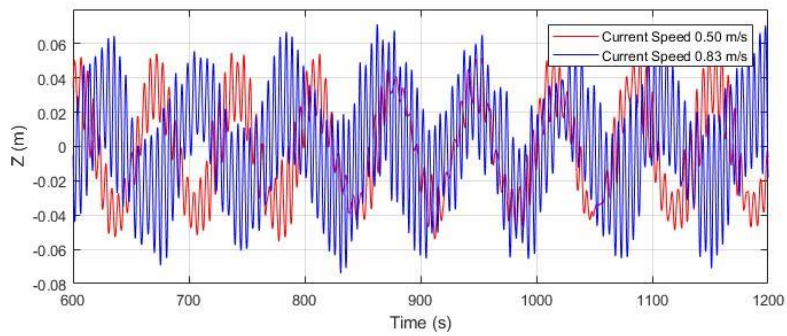


Fig. 23 Cross-flow Motion History

The prescribed motion frequency is 0.0132 Hz for 0.5 m/s and 0.0191 Hz for 0.83 m/s. Clearly, these first two peaks are related to the prescribed motion. The second peak occurs at 0.18 Hz for current speed 0.50 m/s and 0.2 Hz for current speed 0.83 m/s. This frequency is related to the vortex-induced vibration.

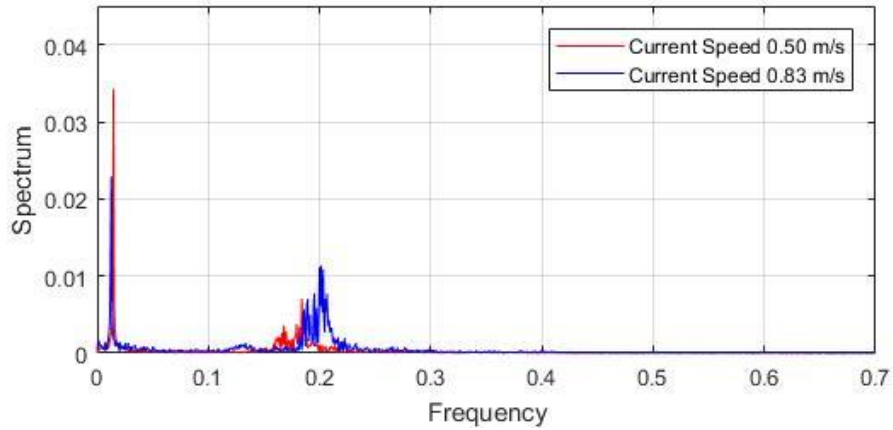


Fig. 24 Spectrum of Motion at Bottom of Riser (CFD)

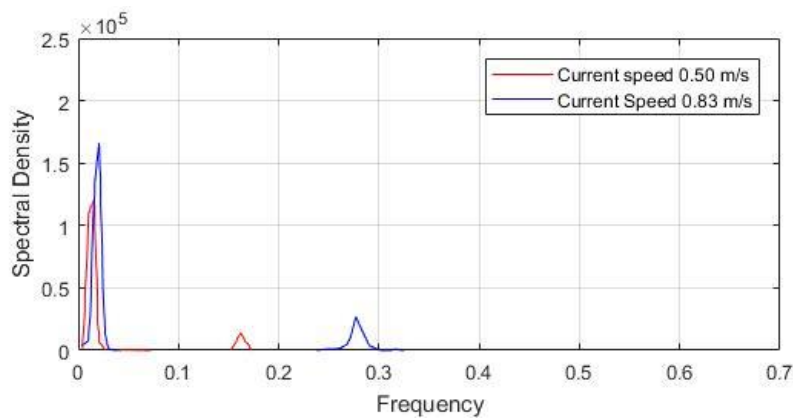


Fig. 25 Spectrum of Cross-flow Loads at Bottom of Riser (Wilde 2007)

Wilde (2007) gives the similar pattern for the cross-flow loads at bottom of riser, as shown in Fig. 25. For the second peaks occurred near 0.2 Hz, it can be attributed to the dynamic coupling between the air can and the riser.

One thing should be clarified is that our CFD simulation did not calculate the load at the bottom of the riser. Because we apply boundary condition there. The spectrum we have reflects the near bottom motion of the riser, while Wilde (2007) only provides Cross-flow Loads at the bottom of the riser.

Wilde (2007) observed trajectory for the buoyancy can only and did not investigate the movement of the riser. In our simulation, the trajectory at bottom of the riser is presented in Fig. 26. This trajectory is quite different with what we usually observe in VIV research. It is not in “figure eight” or “banana shape”. In fact, it is a combination of two shapes. First the riser follows the prescribed motion which is a large “banana shape”. Then, due to the VIV, the riser also has a “figure eight” motion with much smaller amplitude. Thus, we can see an overall “banana shape” consisting of many small irregular “figure eight”. As noted earlier, Wilde (2007) provided only the buoyancy can movement without showing the riser trajectory.

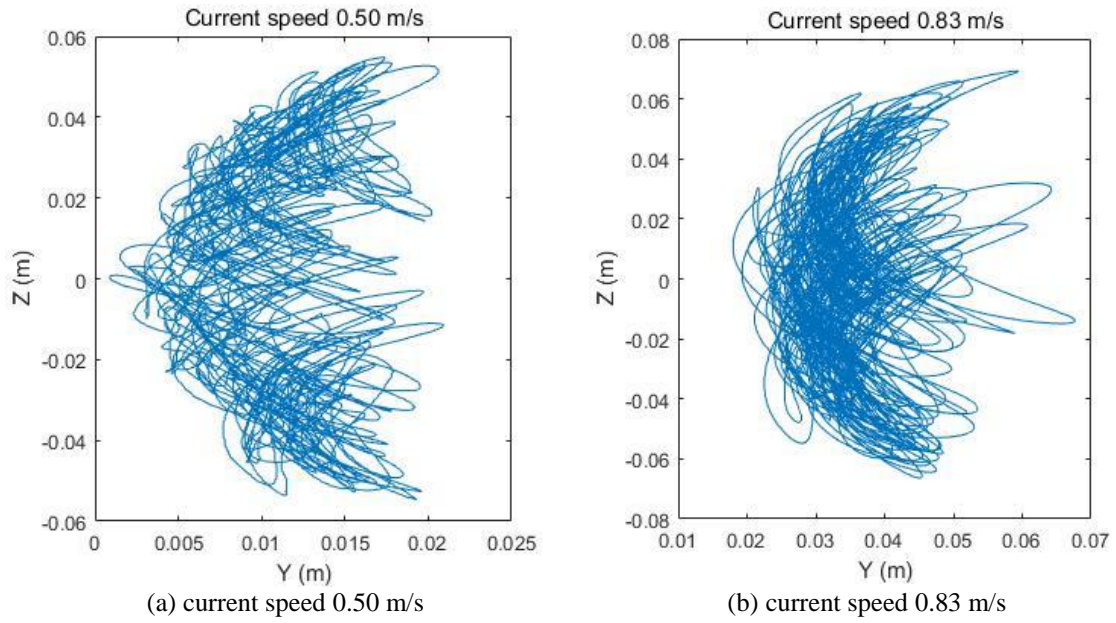


Fig. 26 Trajectory at bottom

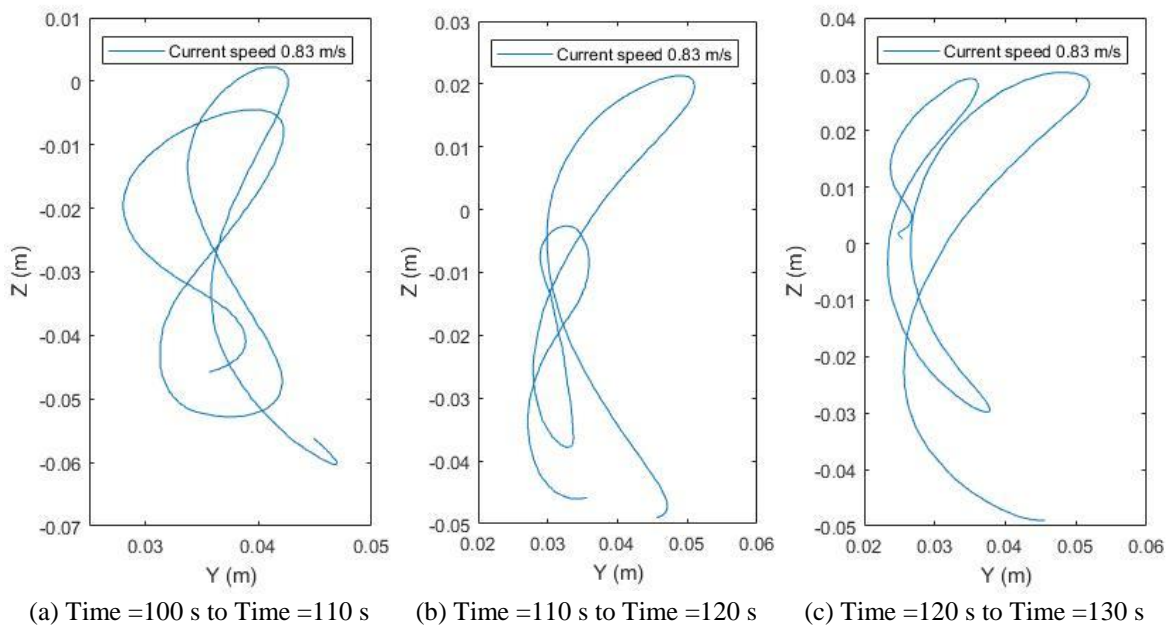


Fig. 27 Trajectory for Current Speed 0.83 m/s

If we plot the trajectory with only a few time steps, we can observe the small “figure eight” more clearly. For example, Fig. 27(a) shows the trajectory for current speed 0.83 m/s during time =100 s to time =110 s. The riser is doing “figure eight” motion with  $z$  roughly ranging from -0.06 m to 0.01 m. Fig. 27(b) shows the following 10 seconds of the trajectory. And Fig. 27(c) shows the next 10 seconds of the trajectory. The trajectories are following “banana shape” or “figure eight” and the mean position of the oscillation is moving upward in  $z$  direction. This phenomenon helps illustrate that the trajectories shown in Fig. 26 are consisting of one prescribed “banana shape” and the small “figure eight” caused by VIV.

Figs. 28-31 show the trajectories at 0.2 L, 0.4 L, 0.6 L and 0.8 L of the Riser. As the location approaches to the top, the prescribed motion become increasingly dominant and the influence of vortex-induced vibration become decreasingly effective. These figures also help illustrate that the trajectories are combined with two shapes of motion.

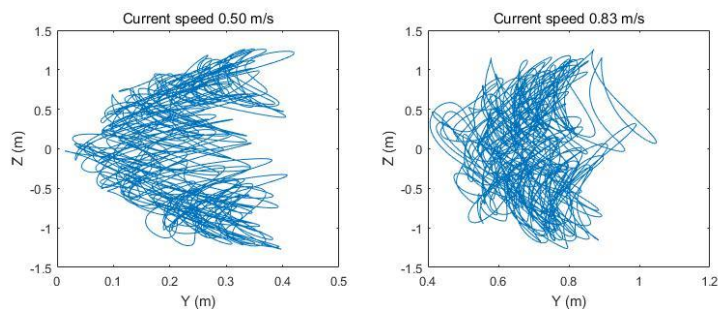


Fig. 28 Trajectories at 0.2 L of Riser

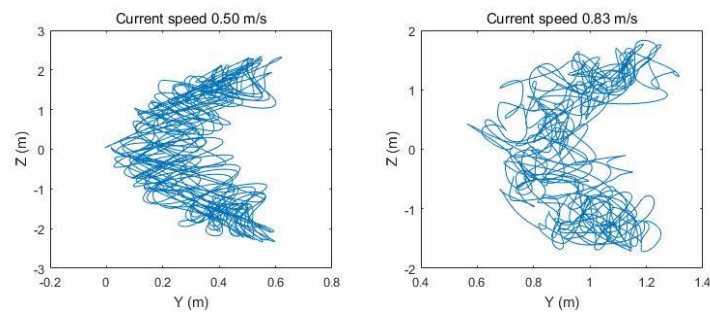


Fig. 29 Trajectories at 0.4 L of Riser

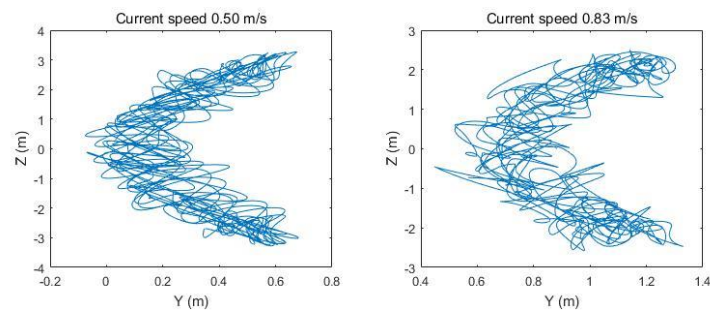


Fig. 30 Trajectories at 0.6 L of Riser

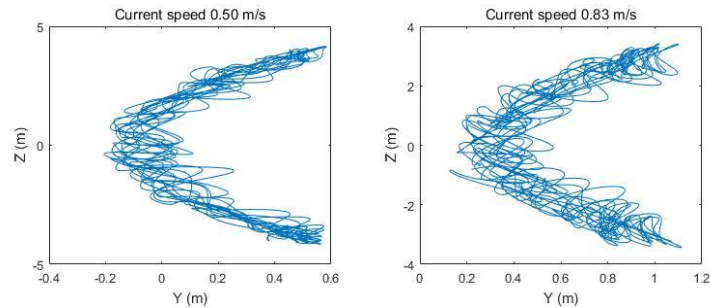


Fig. 31 Trajectories at 0.8 L of Riser

#### 4. VIV simulation of a riser under regular wave

In many previous riser VIV simulations, the riser was assumed to be fixed on two sides. However, in reality, it is not always the case. Attached to the platform, the top of the Riser will move with the platform. In the next part of the paper, we study a riser which is connected to the platform. The coupled system is under harmonic regular wave. No current is applied. We simplify the case by prescribing a sinusoid motion at the top of the riser to replace the platform motion. Parameters from Wilde (2007) were used as reference. For a 300 m depth TLP vibration, the amplitude is about 5 m and the frequency is below 1 Hz (Adrezin *et al.* 1999). The sinusoid motion is prescribed in  $z$  direction, with an amplitude of 5 m, and a frequency of 0.083 rad/s.

##### 4.1 Grid generation

Before CFD calculation, a new grid needs to be generated for this specific case. Since there is no current coming in  $y$ -direction, vortex shedding in  $y$ -direction won't be as remarkable as before. Thus, in order to improve computational efficiency, we can narrow the dimension in  $y$  direction and move the riser to the center of the grid.

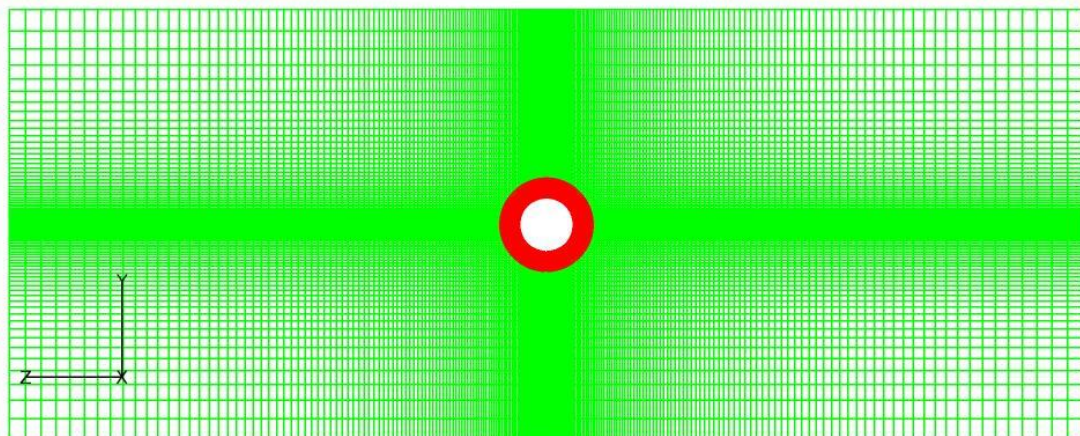


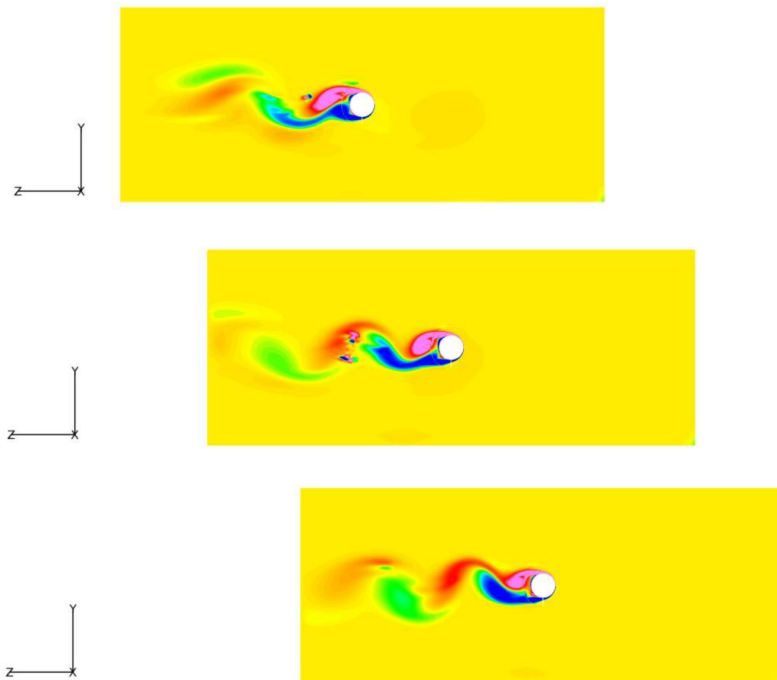
Fig. 32 Overset Grid for VIV Simulation of Riser under Regular Wave

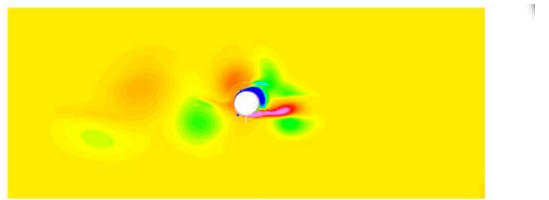
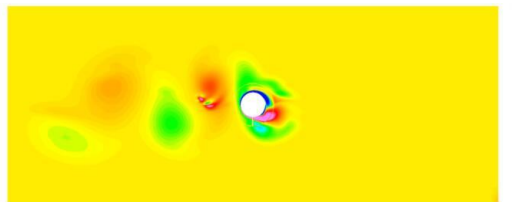
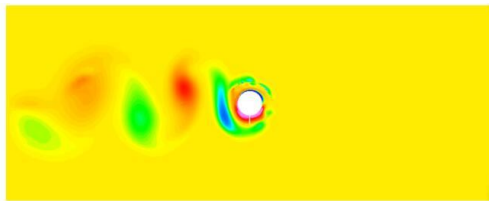
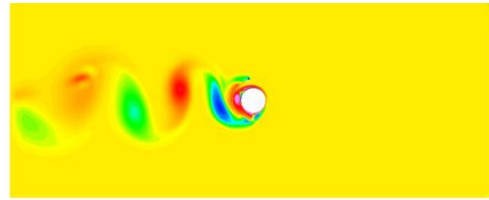
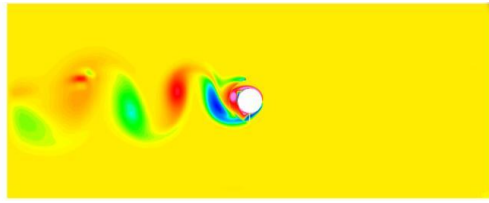
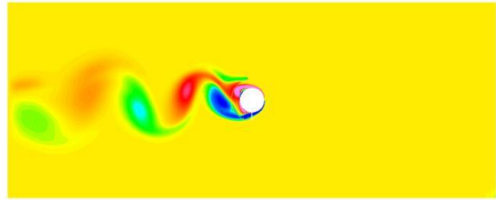
The new grid is shown in Fig. 32. The riser was put at the center of the grid. The grid is  $16 D$  (Diameter of the Riser) in  $y$ -direction and  $40 D$  in  $z$ -direction. Red block consists of 373100 ( $50 \times 182 \times 41$ ) grid points and green block consists of 854550 ( $50 \times 81 \times 211$ ) grid points. There are about 1.2 million computational nodes in this simulation.

For the near body grid, we set the size as  $0.001 D$ . As it departs from the wall, the grid size gradually increases to  $0.025 D$  at the intersection with the wake grid. For green block, the grid size is  $0.025 D$  in the middle and  $0.4 D$  at the far way area in  $y$ -direction. As for  $z$ -direction, the grid size ranges from  $0.025 D$  to  $0.3 D$ . The interpolation between two blocks is guaranteed.

#### 4.2 Simulation results

Fig. 33 shows the motion on the top of the Riser. Due to the sinusoid motion prescribed, vortex sheds behind the Riser. It can be observed clearly, that vortex shedding is related to the speed of the oscillation. The relative speed reaches a maximum when the riser is passing the center of the harmonic vibration and the vortex leaves the riser very quickly. After that point, the riser start to decelerate, and the speed of vortex shedding also slows down. When the riser finally stops, vortex shedding also stops. Then the riser starts to move back, breaking the vortex generated before, creating new vortex.





Continued-

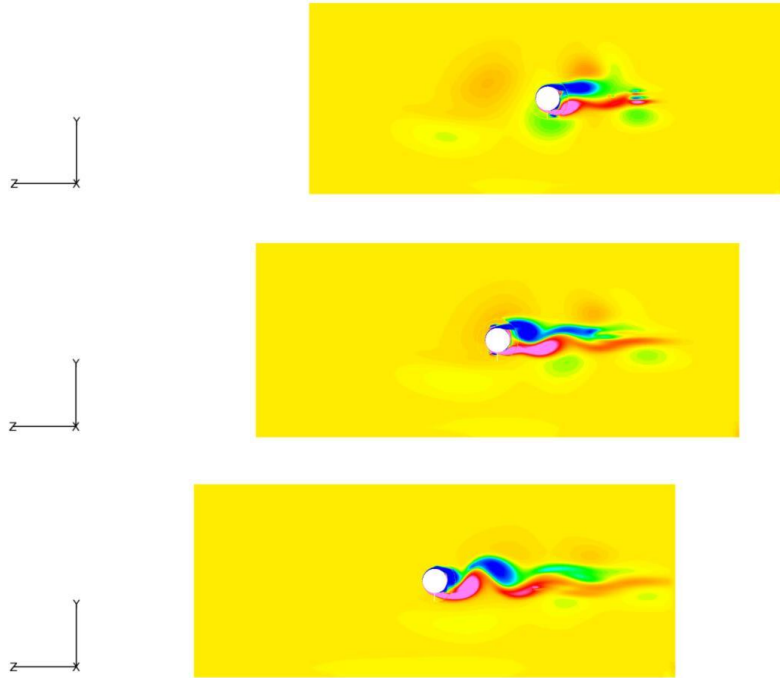


Fig. 33 Vortex Shedding at top of the Riser

Fig. 34 shows the vibration history in z-direction at lower section of the riser (0.4 L). The reason we choose that location to study is because at the top of riser, the motion is subject to the prescribed motion, while at the bottom, the motion is too small to create vortex. As is shown in the plots, there is no vortex-induced vibration can be visually observed in z direction. The motion in z-direction mostly follows the prescribed vibration. However, we can write z motion in Eq. (9). After subtracting the mean motion, we can clearly observe the VIV fluctuation in Fig. 35.

$$Z = \bar{Z} + Z' \tag{9}$$

where  $\bar{Z} = \bar{A} \sin(\bar{\omega} * t)$  is the mean motion in z-direction, and  $Z$  is the fluctuation of the motion.

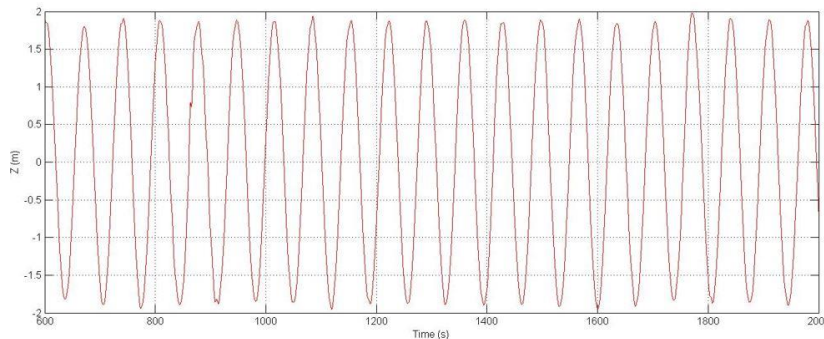


Fig. 34 Motion History in Z-Direction

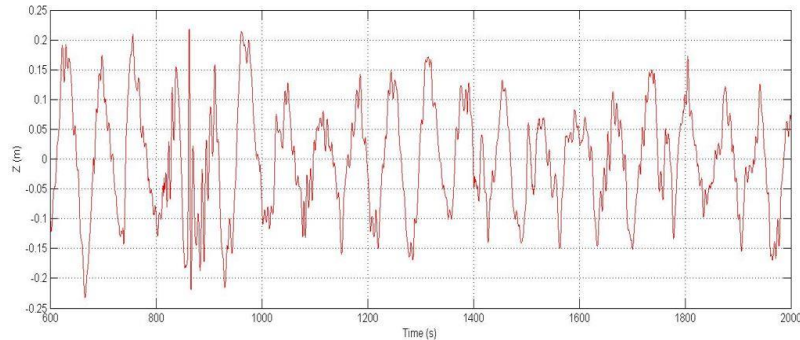


Fig. 35 Small-Amplitude VIV in Z-Direction

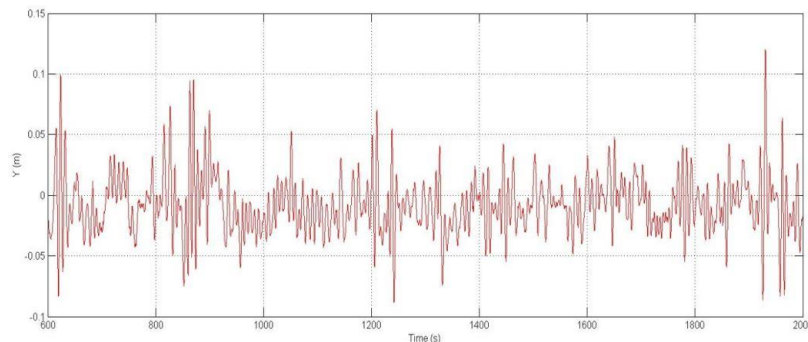


Fig. 36 Motion History in Y-Direction

While in  $y$ -direction, in the absence of prescribed motion, VIV can be observed easily as shown in Fig. 36. The motion mostly ranges from  $-0.1$  m to  $0.1$  m. No distinguishable frequency is observed in this case.

The results were analyzed using a FFT (Fast Fourier Transform) to study the motion in  $y$ -direction. As shown in Fig. 37, most of the peaks occur from  $0$  Hz to  $0.15$  Hz. There is a rough “V” shape for the spectrum in the range from  $0$  Hz to  $0.15$  Hz. Still there is no main frequency can be found. A possible explanation is that due to the sinusoid oscillation, there will be no steady relative velocity between riser and the fluid. It is like constantly varying current passing the riser, the VIV is expected to be irregular.

The trajectory of the motion is presented in Fig. 38. The riser is mainly following the prescribed motion in  $z$ -direction. Vortex-induced vibration in  $y$ -direction is relatively small compared to the motion in  $z$ -direction. At right and left ends of the oscillation, due to the prescribed motion velocity decreasing to zero, riser stays longer at these locations. Thus, there are more vibrations in  $y$ -direction at two ends. Also due to the relative small velocity between riser and flow at these areas, the amplitude of the VIV is relatively small. Riser is moving backward and breaking the vortex generated before. Thus the vibration tends to be more chaotic at these locations.

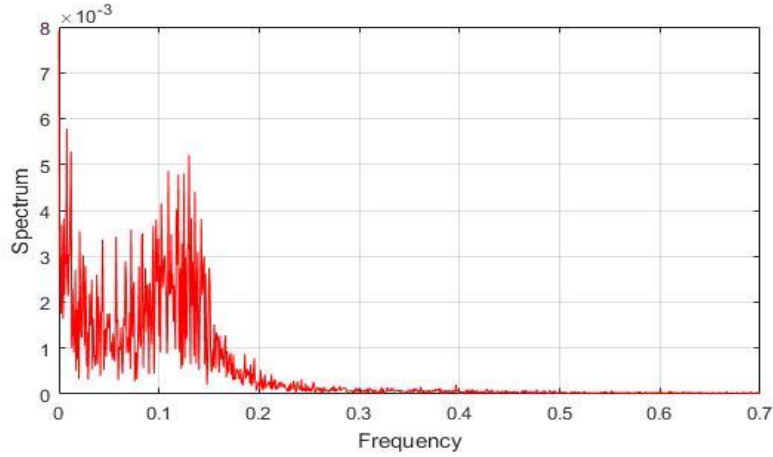


Fig. 37 Frequency in Y Direction

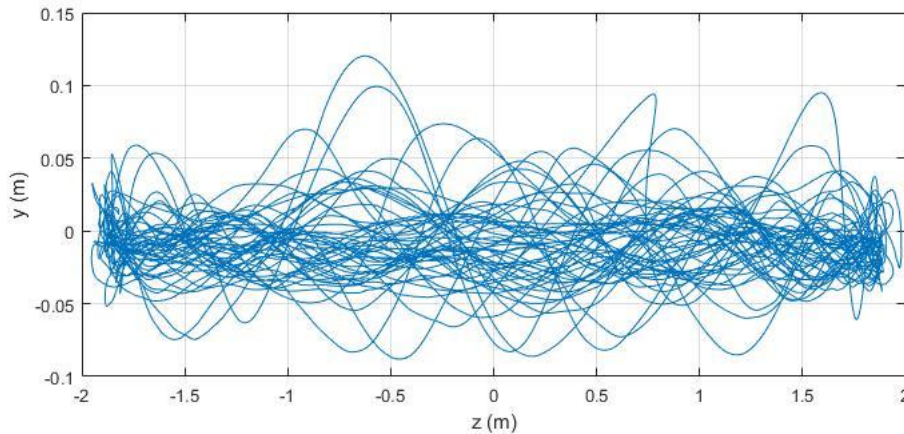


Fig. 38 Trajectory of the Riser

## 5. Conclusions

In this paper, we first developed a riser motion solver by discretizing tensioned beam governing equations. Then we coupled the motion solver with a three-dimensional CFD solver to achieve Fluid-Structure Interactions. Overset grid and dynamic grid techniques are adopted in the CFD approach to facilitate time-domain simulation of the riser motion without tedious and time-consuming grid regeneration.

First case of the simulation is based on Wilde's model test on the VIV of the air can of a FSHR. The simulation simplifies the case by using prescribed motion to replace the motion of the air can. All the input riser parameters are based on the experiment including diameters, length, Young's modulus, weight per length, tension, etc. The in-line and cross-flow motion history, VIV amplitude and frequency, and riser trajectory have been investigated. The results indicate that the riser is subject

to both the prescribed motion and the vortex-induced vibration. Thus the trajectory of the riser is different with the common “figure eight” or “banana shape”. It is a combination of the prescribed “banana shape” and the vortex-induced “figure eight”.

Second case is to simulate a riser connected with a platform, while the platform is under a harmonic regular wave. No current is applied. Still, we simplify the case by prescribing a sinusoid motion in z-direction to replace the movement of the platform. The riser input parameters we use are the same as the one in Wilde’s experiment. Vortex is generated behind the riser as it moves. The faster riser moves, the faster vortex sheds. VIV can be found in both y- and z-directions. Complex vibration appears at two ends, where the riser moves backwards and breaks the previous vortex.

In conclusion, a fully three-dimensional CFD approach for VIV simulation for a top side moving riser has been presented. The riser VIV response is computed in according to the unsteady, incompressible Navier-Stokes equations in conjunction with a large eddy simulation model. The numerical simulation results shed some light on the FSHR VIV problems.

## References

- Adrezin, R. and Benaroya, H. (1999), “Non-linear stochastic dynamics of tension leg platforms”, *J. Sound Vib.*, **220**(1), 27-65.
- Chen, H.C. and Patel, V.C. (1988), “Near-wall turbulence models for complex flows including separation”, *AIAA J.*, **26**(6), 641-648.
- Chen, H.C. and Patel, V.C. (1989), “The flow around wing-body junctions”, *Symposium on Numerical and Physical Aspects of Aerodynamic Flows*, 4th, Long Beach, CA.
- Chen, H.C., Chen, C.R. and Huang, K. (2013), “CFD simulation of vortex-induced and wake-induced vibrations of dual vertical risers”, *Proceedings of the 23th International Offshore and Polar Engineering Conference*.
- Chen, H.C., Patel, V.C. and Ju, S. (1990), “Solutions of Reynolds-averaged Navier-Stokes equations for three-dimensional incompressible flows”, *J. Comput. Phys.*, **88**(2), 305-336.
- Cheng, Y.M. and Lambrakos, K.F. (2006), “Time domain computation of riser VIV from vessel motions”, *Proceedings of the 25th International Conference on Offshore Mechanics and Arctic Engineering*, American Society of Mechanical Engineers.
- Cheng, Y.M. and Lambrakos, K.F. (2007), “Time domain riser VIV predictions compared to field and laboratory test data”, *Proceedings of the ASME 2007 26th International Conference on Offshore Mechanics and Arctic Engineering*, American Society of Mechanical Engineers.
- Huang, K., Chen, H.C. and Chen, C.R. (2007), “Riser VIV analysis by a CFD approach”, *Proceedings of the 17th International Offshore and Polar Engineering Conference. International Society of Offshore and Polar Engineers*.
- Huang, K., Chen, H.C. and Chen, C.R. (2008), “Riser VIV induced fatigue assessment by a CFD approach”, *Proceedings of the 18th International Offshore and Polar Engineering Conference*, International Society of Offshore and Polar Engineers.
- Huang, K., Chen, H.C. and Chen, C.R. (2011), “Numerical scheme for riser motion calculation during 3-D VIV simulation”, *J. Fluid. Struct.*, **27**(7), 947-961.
- Huang, K., Chen, H.C. and Chen, C.R. (2012), “Vertical riser VIV simulation in sheared current”, *Int. J. Offshore Polar Eng.*, **22**(2).
- Liu, N., Cheng, Y., Wilde, J.D., Burke, R. and Lambrakos, K.F. (2009), “Time domain VIV Analysis of a free standing hybrid riser”, *Proceedings of the ASME 2009 28th International Conference on Ocean, Offshore and Arctic Engineering*, American Society of Mechanical Engineers.
- Pereira, P.S.D., Maeda, K., Morooka, C.K., Tamura, K. and Itoh, K. (2005), “Experimental study on a self standing hybrid riser system throughout tests on a deep-sea model basin”, *Proceedings of the ASME 2005*

- 24th International Conference on Offshore Mechanics and Arctic Engineering*, American Society of Mechanical Engineers.
- Pontaza, J.P., Chen, C.R. and Chen, H.C. (2005), "Simulation of high Reynolds number flow past arrays of circular cylinders undergoing vortex-induced vibrations", *Proceedings of the 15th International Offshore and Polar Engineering Conference*, International Society of Offshore and Polar Engineers.
- Pontaza, J.P., Chen, C.R. and Chen, H.C. (2006), "Chimera Reynolds-averaged Navier-Stokes simulations of vortex-induced vibration of circular cylinders", *Civil Engineering in the Oceans VI*, 166-176.
- Rakshit, T., Atluri, S. and Dalton, C. (2008), "VIV of a composite riser at moderate Reynolds number using CFD", *J. Offshore Mech. Arct.*, **130**(1), 011009.
- Rehman, M.U., Vuik, C. and Segal, G. (2007), "Preconditioners for the incompressible Navier-Stokes equations", Delft University of Technology.
- Song, R.X., Stanton, P. and Zhou, X. L. (2010), "Engineering design of deepwater free standing hybrid riser", *Proceedings of the ASME 2010 29th International Conference on Ocean, Offshore and Arctic Engineering*, American Society of Mechanical Engineers.
- Wang, J.S., Liu, H., Jiang, S.Q., Xu, L.B. and Zhao, P.L. (2010), "Vortex-induced vibration on 2D circular riser using a high resolution numerical scheme", *J. Hydrodynamics*, **22**(5), 954-959.
- Wilde, J. (2007), "Model tests on the vortex induced motions of the air can of a free standing riser system in current", *Proceedings of the DOT Conference*.
- Xiao, F. (2015), "CFD simulation of vortex-induced vibrations of free span pipelines including pipe-soil interactions", Diss. Texas A&M University.